

Abstract	I
Acknowledgements	III
Table of Content	V
List of Tables	VIII
List of Figures	IX
Chapter One IR-VUV Photoionization Spectroscopy	
1.1 Introduction	1
1.2 Vacuum-Ultraviolet-Ionization Detected-Infrared Predissociation Spectroscopy (VUV-ID-IRPDS).....	4
1.3 IR-VUV Photoionization Spectroscopy (IR-VUV-PI).....	5
References	9
Chapter Two IR-VUV Photoionization Experiments	
2.1 Introduction	12
2.1.1 VUV-Ionization Detected-IR Predissociation (VUV-ID-IRPD).....	12
2.1.2 IR-VUV Photoionization (IR-VUV PI).....	13
2.2 The Basic Concepts and Details of Construction of Experiments	14
2.2.1 Light Sources	14
Coherent VUV Laser Radiation.....	14
2.2.1.1 VUV Radiation at 118 nm From Nonresonant Third-Harmonic Generation	14
(1) Theory	14
(2) Experiment	17
2.2.1.2 Tunable VUV Radiation Generated With Resonant Four-Wave Mixing.....	18
(1) Theory	18
(2) Experiment	22
2.2.1.3 IR Optical Parametric Oscillator/Amplifier (OPO/OPA) Laser System ...	25

2.2.1.4	Photolysis Laser	28
2.2.2	Time-of-Flight Spectrometer	28
2.2.2.1	Supersonic Jet System	29
2.2.2.2	Linear Time-of-Flight Tube (TOF).....	30
2.2.2.3	Microchannel Plate (MCP) Detector Assembly	31
2.2.2.4	The Total Flight Time.....	31
2.2.3	Data Acquisition	33
	References.....	54

Chapter Three Infrared absorption of methanol clusters (CH₃OH)_n with n = 2–6 recorded with a time-of-flight mass spectrometer using IR depletion and VUV ionization

3.1	Introduction.....	56
3.2	Experiments	58
3.3	Computational Details	60
3.4	Results and Discussion	61
3.4.1	TOF Mass Spectrum of Methanol Clusters	61
3.4.2	Action Spectra as The IR Laser Is Turned.....	63
3.4.3	IR Spectra of (CH ₃ OH) _n	65
3.4.4	Spectral Assignments and Comparisons.....	69
3.5	Conclusion	73
	References.....	83

Chapter Four Infrared spectrum of mass-selected CH₃S radical investigated with infrared + vacuum ultraviolet photoionization

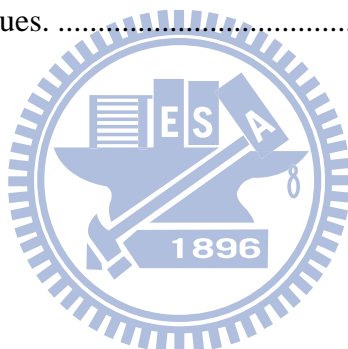
4.1	Introduction.....	87
4.2	Experiments	90
4.3	Results and Discussion	93
4.3.1	Photoionization Efficiency (PIE) Spectra of CH ₃ S	93
4.3.2	Time-of-flight mass spectrum.....	95
4.3.3	IR-VUV spectrum of CH ₃ S	96
4.4	Conclusion	100
	References.....	108

Chapter Five	Vibrational Stark Spectral Studies of DMANB Doped in a PMMA Film	
5.1	Introduction	111
5.2	Theory	114
5.2.1	Effect of Electric Field on Absorption Spectra.....	114
5.2.2	Derive Values of $ \Delta\mu $ and $\Delta\bar{\alpha}$	117
5.3	Material and Methods	119
5.3.1	Sample Preparation	119
5.3.2	Rapid Scan FTIR	120
5.4	Results and Discussion	121
5.5	Conclusion	126
	References.....	144
Appendix A	146
Appendix B	148



List of Tables

Table	page
Table 2-1 Optimum pressures and conversion efficiencies for third-harmonic generation.	35
Table 2-2 Data sheet for type 1 BBO crystal used for doubling the 425.112 nm light.....	36
Table 3-1 Comparison of experimental IR absorption wavenumbers (in cm^{-1}) in the OH-stretching region with theoretical results.....	74
Table 3-2 Comparison of experimental IR absorption wavenumbers (in cm^{-1}) in the CH-stretching region with theoretical results.	76
Table 4-1 Vibrational wavenumbers (in cm^{-1}) of CH_3S observed experimentally and predicted quantum-chemically.....	102
Table 5-1 Comparison of vibrational Stark effect data of the $\text{C}\equiv\text{N}$ stretching mode with literature values.	129



List of Figures

Figure	page
Figure 1-1 Two excitation schemes for IR-VUV ionization. (a) VUV-ionization detected-IR predissociation spectroscopy (VUV-ID-IRPDS). (b) IR-VUV photoionization spectroscopy (IR-VUV-PI).....	8
Figure 2-1 (a) A schematic diagram of the experimental apparatus of VUV-ID-IRPDS using 118 nm light as the VUV source. (b) Picture of the alignment of IR and UV laser beams at the position of ionization region. The distance between two beams is about 3 mm, when the delay time between IR and VUV lights was set to be 30 ns. (c) The intensity of VUV light measured with a copper photoelectric detector.	37
Figure 2-2 (a) The schematic diagram of the experimental apparatus of IR-VUV-PI using a tunable VUV light. (b) The observed optogalvanic signal. When the frequency of UV light is resonant with the two-photon Kr transition, maximum optogalvanic signal is obtained.	38
Figure 2-3 Schematic diagrams of (a) a nonresonant third harmonic generation process at the fundamental laser frequency ω , where $\omega_1 = \omega_2 = \omega_3 = \omega$ and $\omega_{VUV} = 3\omega$ and (b) a four-level system indicating the relevant energy levels for both four-wave sum frequency at $2\omega_1 + \omega_2$, and four-wave difference mixing at $2\omega_1 - \omega_2$. The real levels are labeled $ a\rangle$, $ b\rangle$, $ c\rangle$, and $ g\rangle$, I. P. = ionization potential and imaginary levels are present as solid line and dashed line, respectively. Real levels are labeled $ a\rangle$, $ b\rangle$, $ c\rangle$, and $ g\rangle$. I. P. = ionization potential.	39
Figure 2-4 The 118.2-nm output power as a function of the pressure of added Ar in the tripling cell. The input 354.7-nm beam is in unfocused geometry. (From Ref. 9).....	40
Figure 2-5 The phase-matching factors versus $F_1 b\Delta k$ in the case of tight focusing, for $b/L=0$ and $f/L=0.5$. (a) $F_{\text{sum}}(b\Delta k)$ versus $b\Delta k$. The upper trace is the derivative of $F_{\text{sum}}(b\Delta k)$. (b) $F_{\text{diff}}(b\Delta k)$ versus $b\Delta k$. $F_{\text{sum}}(b\Delta k)$ and $F_{\text{diff}}(b\Delta k)$ are the phase-matching factor in sum- and difference-frequency schemes.....	41
Figure 2-6 Energy level diagrams of relevant atomic levels of nonlinear media of Hg,	

	Xe, Kr, and Ar for the generation of coherent VUV light via two-photon resonance four-wave sum and difference frequency mixing. The wavelength regions are indicated in nm. I.P. denotes the ionization limit of a non-linear medium.....	42
Figure 2-7	Wavelength dependence of the power of the VUV light produced by the difference frequency conversion ($\omega_{\text{VUV}} = 2\omega_1 - \omega_2$) in Kr. ω_1 is fixed at 216.6 nm which is resonant with the two-photon Kr transition $4p-5p$ [$5/2, 2$]. (a) ω_2 is in the range 540–737 nm produced by the fundamental output of the following laser dyes: <i>a</i> , Fluoresceine 27; <i>b</i> , Rhodamine 6G; <i>c</i> , Rhodamine 610; <i>d</i> , Rhodamine 620; <i>e</i> , Rhodamine 640; <i>f</i> , Sulforhodamine; <i>g</i> , DCM; and <i>h</i> , Pyridin 1. (b) ω_2 is in the range 416–550 nm produced by the fundamental output of the following laser dyes: <i>i</i> , Stilbene 420; <i>j</i> , Coumarin 440; <i>k</i> , Coumarin 460; <i>l</i> , Coumarin 480; <i>m</i> , Coumarin 500. (c) ω_2 is in the range 272–360 nm produced by the second harmonic generation of with the same laser dyes as listed in (a). The VUV power is plotted in arbitrary units. The tuning curves are not displayed on the same scale. (From Ref. 14).....	43
Figure 2-8	A detailed schematic diagram for generation tunable VUV light by resonance enhanced four-wave difference frequency mixing ($\omega_{\text{VUV}} = 2\omega_1 - \omega_2$) in a Kr/Ar gas cell via the Kr $4P \rightarrow 5P$ transition at $94,092.86 \text{ cm}^{-1}$ ($= 2\omega_1$). ω_1 (212.556 nm) is generated by doubling of the laser output from a Stilbene 420 dye (425.112 nm).....	44
Figure 2-9	A schematic diagram for measurements of the optogalvanic spectra.....	45
Figure 2-10	(a) The optogalvanic spectrum recorded with a Fe-Ne cell when scanning the grating position of the dye laser (ω_2) from 510.3 to 514.2 nm with a scan step of 0.025 nm. (b) Stick diagram of vacuum wavelength of transition lines of Ne and Fe atoms (from Ref. 25); only intense transitions are plotted....	46
Figure 2-11	Comparison of derivation from the true wavelength for the wavelength read out of a dye laser calibrated with an optogalvanic cell and a wavemeter.....	47
Figure 2-12	Layout of the IR-OPO/OPA laser system (Laser Vision).	48
Figure 2-13	Output energy of the IR OPO/OPA system and the H_2 Raman shifter system in our lab.....	49
Figure 2-14	The interference spectrum of etalon B with NIR output from OPO cavity. The frequency of NIR was set at 12293 cm^{-1} .The spectrum was taken when	

the seeder of pumping YAG laser was turned on.	50
Figure 2-15 (a) A schematic diagram for measurements of a photoacoustic spectrum. B.S. is a 50:50 beam splitter. (b) FTIR spectrum (resolution = 0.5 cm ⁻¹) and photoacoustic spectrum (broadband mode, resolution = 1.5 cm ⁻¹) of CH ₄ (2900–3200 cm ⁻¹), C ₂ H ₂ (3200–3350 cm ⁻¹), and H ₂ O (3500–3700 cm ⁻¹). The photoacoustic spectrum wasn't normalized with IR intensity.	51
Figure 2-16 A schematic diagram of the time-of-flight spectrometer (TOF).....	52
Figure 2-17 Typical timing sequence in the IR-VUV photoionization measurement. The time axis is not to scale and each device is triggered by the rise-edge.	53
Figure 3-1 Time-of-flight mass spectra of a jet-cooled methanol cluster beam produced from a mixture of CH ₃ OH/He = (1/100) at a stagnation pressure of 850 Torr. (a) ionization at 118 nm; (b) IR irradiation at 2950 cm ⁻¹ applied 200 ns before ionization at 118 nm; (c) IR irradiation at 3150 cm ⁻¹ applied 200 ns prior to ionization at 118 nm. The <i>m/z</i> values for (CH ₃ OH) _{<i>n</i>} H ⁺ and (CH ₃ OH) _{<i>n</i>} ⁺ are indicated.	78
Figure 3-2 Time-of-flight mass spectra (a) and action spectra (b) of a jet-cooled methanol cluster beam produced from a mixture of CH ₃ OH/He = (5/1000) at a stagnation pressure of 800 Torr. The action spectra were recorded on monitoring the fractional variations in intensity of each mass channel as the wavelength of the IR laser was scanned.	79
Figure 3-3 Reaction and ionization scheme of methanol clusters.	80
Figure 3-4 Infrared spectra of (CH ₃ OH) _{<i>n</i>} for <i>n</i> =1–5 derived from action spectra shown in Figure 3-2 according to the dissociation and ionization mechanisms described in text. M indicates CH ₃ OH. The spectrum of M ₆ was obtained in a separate experiment in which (CH ₃ OH) ₆ has a higher concentration.	81
Figure 3-5 Time-of-flight mass spectra (a) of a jet-cooled methanol cluster beam, produced from a mixture of CH ₃ OH/He = (3/100) at a stagnation pressure of 1670 Torr, and IR spectra (b) of (CH ₃ OH) ₄ and (CH ₃ OH) ₅ obtained with the fluence of IR radiation at 4 and 2.5 mJ mm ⁻²	82
Figure 4-1 Normal modes of the CH ₃ S radicals. The a ₁ modes are described approximately as the CH ₃ symmetric stretching (<i>v</i> ₁), the CH ₃ umbrella	

- motion (ν_2), and the C–S stretching (ν_3) modes. The degenerate e modes are the CH_3 asymmetric stretching (ν_4), the CH_3 deformation (ν_5), and the HCS deformation (ν_6) modes. 103
- Figure 4-2 Photoionization efficiency spectra of CH_3S (a) in region 9.14–9.38 eV ($73,719\text{--}75,655\text{ cm}^{-1}$) recorded with scan step 4 cm^{-1} , (b) in region 9.2440–9.2635 eV ($74,558\text{--}74,715\text{ cm}^{-1}$) with scan step 1 cm^{-1} , (c) in region 9.218–9.234 eV ($74,348\text{--}74,477\text{ cm}^{-1}$) with scan step 1 cm^{-1} , and (d) in region 9.30–9.46 eV ($75,010\text{--}76,300\text{ cm}^{-1}$) with scan step 4 cm^{-1} . The insets are first-order derivative spectra fitted with Gaussian functions. The energies of the maxima thus derived are indicated with thick blue arrows. The threshold energies are indicated with thin black arrows. 104
- Figure 4-3 (a) Photoionization efficiency spectra of CH_3SH in region 9.415–9.482 eV, and (b) its first-order derivative spectra fitted with Gaussian function. 105
- Figure 4-4 Time-of-flight spectra of a supersonic jet of Ne containing 1 % CH_3SH . (a) ionization with VUV light at 134.84 nm (9.195 eV, $74,165\text{ cm}^{-1}$), (b) ionization with VUV light at 134.84 nm and IR light at 2905 cm^{-1} applied 200 ns before VUV light, (c) the jet was irradiated with light at 248 nm before ionization with VUV light at 134.84 nm, and (d) the jet was irradiated with light at 248 nm before ionization with VUV light at 134.84 nm and IR light at 2905 cm^{-1} applied 200 ns before VUV light. DMDS⁺ indicate $\text{CH}_3\text{SSCH}_3^+$ 106
- Figure 4-5 Comparison of IR spectra in regions 2790–3020 and 3200–3270 cm^{-1} observed in IR-VUV photoionization experiments with the stick spectrum predicted quantum-chemically. (a) The change in intensity of the CH_3S^+ signal was monitored while the wavenumber of the IR laser was tuned; the wavelength of the VUV laser was maintained at 134.84 nm. (b) Stick diagram of transition wavenumbers predicted in Ref. ; the wavenumbers are scaled by 0.959 and the statures reflect predicted relative IR intensities. Vibrational transitions from CH_3S ($X^2E_{3/2}$) are indicated in red and those from CH_3S ($X^2E_{1/2}$) are in blue, with half stature to reflect likely population relative to CH_3S ($X^2E_{3/2}$) upon photolysis of CH_3SH at 248 nm. 107
- Figure 5-1 (a) Two possible mechanisms of intramolecular charge transfer process. The

	structures of twisted intramolecular charge transfer (TICT) state and the planar intramolecular charge transfer (PICT) state are shown. (b) Schematic illustration of the processes and states involved in the photophysics of DMABN according to the mechanism of twisted intramolecular charge transfer.	129
Figure 5-2	Schematic illustration of effects of an applied electric field on the shape of an absorption line. (a) Molecules of which $\Delta\bar{\mu}$ (shown here for $\Delta\bar{\mu}>0$) is oriented parallel or antiparallel to the electric field \mathbf{F} have their transition energy shifted to smaller or greater energy, respectively. The consequence for the absorption spectrum (solid and dashed lines denote the spectrum without and with an applied electric field) is shown on the right: some orientational subpopulations are shifted to smaller energy, some to greater energy, and some remain the same, resulting in a broadened band. The Stark spectrum has a second derivative line shape as shown. (b) The applied field induces a dipole moment that is typically in the direction of the applied field, regardless of the orientation of the molecule. The absorption energy shifts towards smaller or greater energy depending on $\Delta\alpha>0$ or $\Delta\alpha<0$, and a line in the Stark spectrum has a positive or negative first-derivative shape.....	130
Figure 5-3	Chemical structures of PMMA and DMABN.	131
Figure 5-4	Schematic illustration of the device. (a) The side view. (b) The top view.....	132
Figure 5-5	(a) Experimental setup for vibrational Stark spectroscopy. BS, FM, and MM represent the KBr beamsplitter, fixed mirror, and moving mirror, respectively. (b) Timing chart for the measurement using the DC electric field method in rapid-scan mode.	133
Figure 5-6	(a) IR absorption spectrum and (b) vibrational Stark spectrum of PMMA ($\chi = 90^\circ$). The applied electric field is 0.875 MV cm^{-1}	134
Figure 5-7	(a) Vibrational Stark spectrum of PMMA in the C=O stretching region at three applied fields ($\chi = 90^\circ$), $\mathbf{F} = 0.75, 0.875, \text{ and } 1.25 \text{ MV cm}^{-1}$. (b) The peak height of Stark signal as a function of the square of the applied electric field.....	135
Figure 5-8	(a) Vibrational Stark spectrum of PMMA in the C-O-C and C-C stretching region at three applied field ($\chi = 90^\circ$), $\mathbf{F} = 0.75, 0.875, \text{ and } 1.25 \text{ MV cm}^{-1}$. (b) The peak height of Stark signals at $1147 \text{ and } 1239 \text{ cm}^{-1}$ (marked * in (a))	

	as a function of the square of the applied electric field.	136
Figure 5-9	(a) IR absorption spectrum and (b) vibrational Stark spectrum of DMABN doped in a PMMA film ($\chi = 90^\circ$). DMABN:PMMA=1:2. The applied electric field is 1.0 MV cm^{-1}	137
Figure 5-10	(a) Vibrational Stark spectra, under the condition of the magic angle, collected with 200 and 700 loops. The applied electric field is 1.2 MV cm^{-1} . (b) The residual spectrum obtained on subtracting the spectrum for 200 loops from the twice spectrum for 700 loops.	138
Figure 5-11	Vibrational Stark spectra of DMABN doped in a PMMA film. (a) $\chi = 90^\circ$ and (b) $\chi = 54.7^\circ$. The applied electric field is 1.2 MV cm^{-1}	139
Figure 5-12	(a) Comparison of vibrational Stark spectrum (field on minus field off) and simulated spectrum of PMMA for the C=O stretching mode ($\chi = 90^\circ$). The applied electric field is 1.0 MV cm^{-1} . The red circles represent the data; solid line represents a fit. (b) Absorption spectrum of PMMA. (c) Solid, dot, and dashed dot lines are contributions of the zeroth-, first- and second-derivatives.	140
Figure 5-13	(a) Comparison of vibrational Stark spectrum and simulated spectrum of DMABN for the C \equiv N stretching mode ($\chi = 90^\circ$). The applied electric field is 1.0 MV cm^{-1} . The red circles represent the data; solid line represents a fit. (b) Absorption spectrum of DMABN. (c) Solid, dot, and dashed dot lines are contributions of the zeroth-, first- and second- derivatives.	141
Figure 5-14	(a) Comparison of vibrational Stark spectrum and simulated spectrum of PMMA for the C=O stretching mode ($\chi = 54.7^\circ$). The applied electric field is 1.4 MV cm^{-1} . The red circles represent the data; solid line represents a fit. (b) Absorption spectrum of PMMA. (c) Solid, dot, and dashed dot lines are contributions of the zeroth-, first- and second- derivatives.	142
Figure 5-15	(a) Comparison of vibrational Stark spectrum and simulated spectrum of DMABN for the C \equiv N stretching mode ($\chi = 90^\circ$). The applied electric field is 1.4 MV cm^{-1} . The red circles represent the data; solid line represents a fit. (b) Absorption spectrum of PMMA. (c) Solid, dot, and dashed dot lines are contributions of the zeroth-, first- and second- derivatives.	143
Figure A-1	Comparison of the VSE spectrum and the simulated spectrum of DMABN doped in a PMMA film for the (a) C=O and (b) C \equiv N stretching modes. ($\chi =$	

90°). The applied electric field is 1.2 MV cm^{-1} 147

Figure A-2 Comparison of the VSE spectrum and the simulated spectrum of DMABN doped in a PMMA film for the (a) C=O and (b) C≡N stretching modes. ($\chi = 54.7^\circ$). The applied electric field is 1.4 MV cm^{-1} 147

